Check for updates

Gold micromeshes as highly active electrocatalysts for methanol oxidation reaction†

Jingying Sun,‡[a] Feng Wang,‡[a] Yuan Liu,[a] Yizhou Ni,[a] Haiqing Zhou,[a] Chuan Fei Guo*[b] and Shuo Chen [ID] *[a]

A high density of surface defects is a key factor for efficient nanoscale gold (Au) electrocatalysts for the oxidation of small organic molecules. Here we present tunable pore size Au micromeshes with a high density of steps, kinks, twin boundaries, and stacking faults fabricated by using a template method. Electrocatalytic measurements on the methanol oxidation reaction show that the peak current density (normalized to the electrochemical surface area) of our Au mesh in alkaline electrolyte (0.5 M KOH) can reach 0.264 mA cm^{-2}, which is significantly higher than those of the well-studied nanoporous Au film (0.081 mA cm^{-2}) and nanoporous Au nanoparticles (0.112 mA cm^{-2}). Over 90% of the current density can be maintained after 500 cycling tests. Through transmission electron microscopy studies, the superior intrinsic activity and stability lie in the high linear density of surface defects, the exposure of active facets, and superficial tensile strain on the outter-most layers.

Introduction

Nanostructured gold (Au) exhibits high activity in oxidizing small molecules, particularly carbon monoxide, methanol, ethanol, and butanol.[1–3] Gold electrocatalysts for all these reactions share a similar mechanism, where high index facets and defects on the Au surface enhance the activity. Here we use our gold micromeshes and methanol oxidation reaction (MOR) as a model system to probe the effect of high index facets and defects on the intrinsic electrocatalytic activity of pure Au micromeshes. In addition, our micromesh structure allows the fabrication of flexible Au electrocatalysts due to the superior mechanical robustness of mesh structures against deformation.[4] Although platinum (Pt) exhibits the highest MOR activity, it can be poisoned by the intermediates formed during the process of MOR. In contrast, Au does not suffer from such poisoning, and is therefore considered as a more promising catalyst for MOR.[5,6] The electrocatalytic activity of Au depends on many factors such as size,[1,7] surface facet,[8] and defect[9,10] involving steps, kinks, stacking faults, twin boundaries, dislocations, *etc.*[11,12] These defects are considered as catalytically

active sites due to their high surface energy, which promotes ionization and adsorption of intermediate reactants, such as OH$^-$ in electrolytes.[13,14] Therefore, precise control over the shape, size, and defect of Au nanostructures is the key to achieving excellent electrocatalytic activity.[7,15]

Among different types of Au nanostructures (nanoparticles, nanowires, *etc.*), porous Au has attracted many interests because of their large surface area, high electrical conductivity, and frequent occurrences of low-coordination facets.[8] The state-of-the-art porous Au films are usually fabricated by dealloying Au–Ag or Au–Cu alloys followed by thermal annealing.[5,16] Although this approach is widely used, it fails to completely remove the residual Ag or Cu, and thus can lead to a reduced catalytic activity compared to pure Au.[17,18] Furthermore, the pore size formed by removing the sacrificial Ag or Cu components is from tens to hundreds of nanometers,[9] which may block mass transport paths and reduce the effective surface area.[19] Moreover, the dealloying approach mainly generates external surface defects such as steps and kinks. There is still plenty room to introduce dense and effective defects inside grains of porous Au, such as stacking faults, dislocations, twins, *etc.*

Here we report a facile route to fabricate large-scale two-dimensional (2D) pure Au micromeshes with tunable pore size by using a template method. The 2D Au nanostructures with micrometer pores can effectively utilize the catalyst surface.[10] Through our materials, intrinsic catalytic activities of Au are investigated, which are superior to that of dealloyed Au.[16] The high activity of Au micromeshes is attributed to high-index surfaces and defects inside grains that are required to accommodate the porous structure of the micromeshes, which are

[a]Department of Physics & The Texas Center for Superconductivity, University of Houston, Houston, Texas 77204, USA. E-mail: schen34@uh.edu

[b]Department of Materials Science & Engineering, South University of Science & Technology of China, Shenzhen, Guangdong 518055, China. E-mail: guocf@sustc.edu.cn

† Electronic supplementary information (ESI) available: CV curves with different scan rate, SEM images of morphology change before and after cycling, TEM images of surface atomic structures, and comparison of electro-oxidation activity among Au nanostructures. See DOI: 10.1039/c7ra02505j

‡ J. S., and F. W. contributed equally.

confirmed by our high-resolution transmission electron microscopy (HRTEM) observation. In addition, our Au micro-mesh exhibits good stability: it remains 90% of activity even after 500 cycles, which is far better than reported results.

Experimental

Au micromeshes fabrication

The micromeshes were fabricated *via* a template method. First, poly(methyl methacrylate) (PMMA) porous film template was prepared *via* a phase separation method induced by nonsolvent (water).[20] A glass slide was dipped into the mixture of tetrahydrofuran (THF)/water/PMMA (mass ratio 25 : 2.5 : 1) and subsequently dried at 75 °C for 15 min. A sacrificial layer of SiO_2 (60 nm) and a layer of Au (50 nm) were deposited successively onto the template by an electron beam evaporation system (Edwards BOC-500). The sacrificial silica layer was dissolved by wedging the glass slide into HF to obtain Au micromeshes[21] (Fig. 1). To characterize the electrocatalytic performance, the micromeshes were transferred to electrochemically inert polydimethylsiloxane (PDMS) substrates.[22] For TEM studies, the Au micromeshes were loaded to copper TEM grids coated with holy carbon films.

Structural characterization

The morphologies of Au micromeshes were characterized by a field-emission scanning electron microscope (FE-SEM, LEO 1512). The surface facets and defects were studied with a high-resolution transmission electron microscope (HRTEM, JEOL 2010F).

X-ray photoelectron spectroscopy

The binding energies of 4f orbit of Au micromeshes and Au film were explored by X-ray photoelectron spectroscopy (XPS, Electronics Model 5700). The data were obtained over a binding energy range of 80–100 eV with the energy increment of 0.1 eV. Each spectrum was averaged by three scans and each peak was base-line corrected by the carbon 1s spectra whose peak energy is 284.5 eV.

Electrochemical measurements

The electrochemical activity of Au micromeshes for MOR was obtained in a standard three-electrode system consisted of a Au micromeshes/PDMS working electrode, a Pt wire counter electrode, and a saturated calomel reference electrode (SCE) in acidic electrolyte or a mercury oxide mercury (Hg/HgO) reference electrode in alkaline environment. All the electrochemical performances of Au micromeshes were conducted using an electrochemical workstation (Biologic SP-200) at room temperature (25 °C). All the potentials presented in the paper were converted to the reversible hydrogen electrode (RHE) scale.

Measurement of electrochemical active surface area (ECSA)

Prior to MOR in alkaline solution, the Au micromeshes were cleaned in Ar-saturated 0.1 M $HClO_4$ solution with a scan rate of 20 mV s^{-1} from 0.65 V to 1.6 V for 30 cycles. The electrochemical active surface area (ECSA) of Au micromeshes working electrodes were calculated by:

$$\mathrm{ECSA} = \frac{Q}{a \cdot v} = \frac{\int I \mathrm{d}U}{a \cdot v}$$

where Q is the charge related to the reduction of AuO layer; I and U are the current and voltage in the CV curves around the AuO striping peak at 1.2 V, respectively; v is the scanning rate; a is the charge per unit area of Au (400 μC cm^{-2}).[23,24] The activities of Au micromeshes for MOR were measured by cyclic voltammetry (CV) in an Ar-saturated mixed solution of 0.5 M KOH and 1 M CH_3OH, in the potential range 0.85 to 1.6 V at the scan rate of 20 mV s^{-1}. The specific activities were normalized by ECSA.
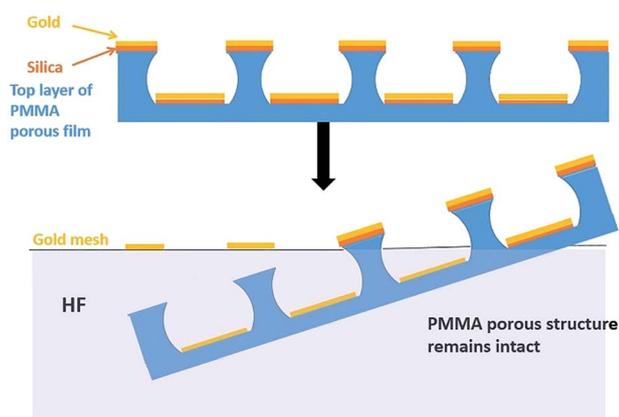

Fig. 1 Schematic process of lifting Au micromeshes from porous template.
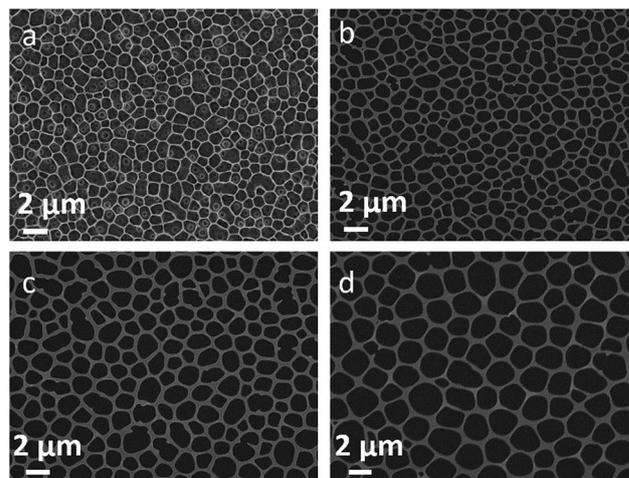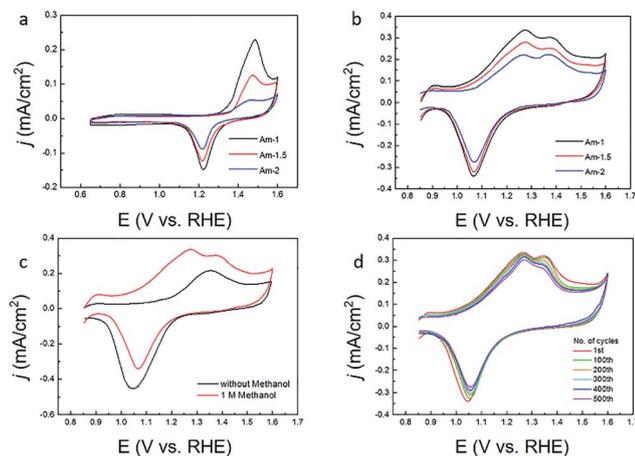

Fig. 2 SEM images of (a) the PMMA template with a pore size of 1 μm and (b) corresponding Au micromeshes. As templates can control pore sizes of Au micromeshes, Au micromeshes with an average pore size of (c) 1.5 μm and (d) 2 μm were further produced using the same method.

Results and discussions

The as-fabricated Au micromeshes typically have a geometric area of 1.5 cm^2 (1 cm × 1.5 cm). Fig. 2 shows some representative SEM images of the as-fabricated Au micromeshes. The Au micromeshes consist of uniform porous structure, which is analogous to the 2D Au nanoporous films made by the dealloying method.[16] In addition, the average pore sizes of Au micromeshes are controlled by the pore sizes of the PMMA template (Fig. 2a) which can further be tuned by changing the PMMA/water ratio. As shown in Fig. 2b–d, with the PMMA concentration being 10%, 8%, and 7%, the corresponding average pore diameters (D_n) are ~1(±0.3) μm, ~1.5(±0.5) μm, and ~2(±0.6) μm. The samples are subsequently named as Am-1, Am-1.5, and Am-2, respectively. The energy-dispersive X-ray spectroscopy (EDS) mapping results indicate that carbon is distributed on the whole SEM image of PMMA template, and Au forms the mesh structure with various pore sizes (Fig. S1 and insets†).

Fig. 3a shows the CV curves of Au micromeshes with different pore sizes in 0.1 M HClO$_4$ solution at a scan rate of 20 mV s^{-1}, from which the ECSA is calculated as 0.606 cm^2, 0.348 cm^2, and 0.313 cm^2 for Am-1, Am-1.5, and Am-2, respectively. The specific activity of Au micromeshes on MOR in 0.5 M KOH and 1 M CH$_3$OH electrolyte is shown in Fig. 3b. Am-1 has the highest activity with the highest peak current density of 0.336 mA cm^{-2}, followed by Am-1.5 with 0.280 mA cm^{-2} and Am-2 with 0.221 mA cm^{-2}. Fig. 3c shows the CV curves from 0.85 to 1.6 V in the alkaline solution with and without methanol of the sample Am-1. In the solution with methanol, the current density reaches a stable maximum of 0.336 mA cm^{-2} at the potential of 1.27 V after several cycles. However, there is no peak observed in the methanol free solution at the same potential.

On the other hand, one smaller peak is observed at 1.37 V in both solutions with/without methanol. Comparing these two CV curves, we conclude that the first oxidation peak at 1.27 V is from the MOR, and the hump located at 1.37 V is associated with Au surface oxidation.[7] The Au oxides are subsequently removed during the negative sweeping scan, yield a reduced peak at 1.05 V.[25] We further confirm the methanol oxidation reaction on the Au micromeshes with different methanol concentrations and various scanning rates in 0.5 M KOH medium. In the typical CVs (Fig. S2a†) taken from various methanol concentrations in 0.5 M KOH on Am-1, the current density increases linearly from 0.275 mA cm^{-2} to 0.510 mA cm^{-2} (Fig. S2b†) with methanol concentration increasing from 0.5 M to 3.0 M. In addition, the higher the methanol concentration, the more negative is the MOR peak position. Fig. S2c and d† show the CV curves of Am-1 in 0.5 M KOH and 1 M CH$_3$OH with different scan rates. Without changing the peak position, the peak current densities increase with the scan rates. An oxidation peak appeared at 1.01 V on the back scanning curve with the scan rate of 5 mV s^{-1}, indicating a continuous methanol oxidation reaction. We also executed MOR experiments on Am-1 in 1.0 M methanol with different KOH concentrations from 0.1 M to 2 M. (Fig. S3†) The peak current also displays an increase in proportion to the KOH concentration, boosting from 0.312 mA cm^{-2} to 0.641 mA cm^{-2}, and the peak position eventually negatively shifts to 1.22 mV in 2.0 M KOH. The peak shift can be attributed to the improved catalytic activity by increasing the coverage of OH$^-$ on the electrode at higher KOH concentrations.[26] In order to compare our results with literature values, we extract the activity from CV curves with the scan rate of 20 mV s^{-1} in the 0.5 M KOH with 1 M CH$_3$OH solution. Subtracting the background current in the methanol-free electrolyte, the peak current densities increase from 0.149 mA cm^{-2} to 0.208 mA cm^{-2} with average pore size decreasing from ~2 μm to ~1.5 μm. Furthermore, when the average pore size decreases from ~2 μm to ~1 μm, the peak current density increases from 0.208 mA cm^{-2} to 0.264 mA cm^{-2}. The electrocatalytic activities (subtracting background) of Au with different morphologies in literatures are compared in Table S1.† The MOR current density of our Am-1 sample (0.264 mA cm^{-2}) is significantly higher than those of all existing Au nanostructures including the trisoctahedron Au nanocrystals (0.139 mA cm^{-2}), the hollow nanoporous Au nanoparticles (0.112 mA cm^{-2}), the nanoporous Au (0.081 mA cm^{-2}), etc. The onset potentials at which the current density reaches 0.01 mA cm^{-2} are also presented in Table S1.† The Au micromeshes achieve the lowest MOR onset/peak potential (V) among all Au nanostructure catalysts.

Next, we discuss the mechanism of high intrinsic activity of our Au micromeshes. In alkaline solution, methanol is oxidized to HCOO$^-$ by OH$^-$ chemisorbed onto the surface of the nanostructured Au with transferring of four electrons at relatively lower potentials (0.85 to 1.45 V) and oxidized to CO$_3^{2-}$ by OH$^-$ with transferring of six electrons at higher potentials (above 1.45 V).[6] However, the intrinsic adsorption ability on Au is weak, resulting in a low-concentration of chemisorbed OH$^-$ anions on the surface and thus a relatively low electrocatalytic activity.[6,17,27]

Fig. 3 Electrochemical performances of Au micromeshes sample. (a) Oxide stripping curves of Au micromeshes with different pore sizes in 0.1 M HClO$_4$ solution. (b) Catalytic methanol electro-oxidation measurements on Am-1, Am-1.5, and Am-2 samples in 0.5 M KOH + 1 M CH$_3$OH solution. (c) CVs of Am-1 electrode on in 0.5 M KOH with and without 1 M CH$_3$OH solution. (d) Repetitive potential cycling in 0.5 M KOH + 1 M CH$_3$OH on Au micromeshes sample with Am-1. The scan rate is 20 mV s^{-1}.

As pointed out by first-principle calculations, the adsorption is closely related to the d-band filling of transition metal catalysts.[28] Higher d-band centre yields less occupation of antibonding state and thus enhances the chemisorption strength (d-band centre theory).[29,30] In our samples, both tensile strain and low-coordinated Au atoms will cause reduction in the overlap of electron cloud of d-band, consequently narrow the Au d-band and upshift the d-band centre.[31] Our XPS results of regular Au film, Am-1, Am-1.5, and Am-2 (Fig. S4†) further confirm the upshift of d-band centre. XPS is much more sensitive to the Au 4f signals than to the Au 5d signals, and the binding energy of d band and 4f core line of Au is correlated, although the absolute values of them differ.[32] So here we use the shift of Au 4f peaks to represent that of Au 5d signals. Our XPS results indicate that the 4f peaks of Au micromeshes samples Am-1, Am-1.5, and Am-2 all have lower binding energy compared with that of Au film. Consequently, the d centres of our Au micromeshes are higher than that of the Au film. Among the three Au micromeshes samples, AM-1 shows the lowest 4f binding energy, indicating a highest d band centre, although the shift is not significant. Such a small change can be attributed to a relatively low contribution of surface facets and strains to the core 4f energy.

To understand the electrocatalytic performance of Au micromeshes, it is essential to characterize their surface morphology. TEM image (Fig. 4a) indicates that the micromeshes consist of grains with 10 to 50 nm diameter. A typical

high-resolution TEM image (Fig. 4b) reveals the abundance of surface steps, dislocations, twin boundaries, and stacking faults (Fig. 4c). In general, for face centre cubic Au, planes with higher surface energy are more catalytic active.[13,33] For example, the 110 (ref. 21) surfaces have higher surface energy (1.94 J m^{-2}) than the 100 and 111 (ref. 34) surfaces (1.80 J m^{-2} and 1.52 J m^{-2}, respectively), and also higher catalytic MOR activity.[8,35,36] The mechanism can be attributed to the stronger adsorptions of intermediate reaction species, such as OH_{ad}^-, and Au–$OH_{ads}^{(1-\lambda)-}$. For stacking faults and dislocations, the atoms in their vicinities have high surface energies, therefore serve as active sites provided that they locate on the out-most atoms layers.[37] In addition, the twin boundaries are also active sites because the atoms in the boundaries possess low-coordination numbers comparing with the internal and close packed atoms.[38]

We also carried out detailed analysis of the surface steps, the most abundant features on our Au micromeshes. A statistical analysis is performed over 1000 steps among 150 HRTEM images to quantify the linear density of defects on the Au micromeshes of different planes along the pore perimeter projected along [101] zone axis. Three representative HRTEM images are shown in Fig. S5†. As a result, the low-index facets, such as (100) and (111), and other defects are frequently observed in all the images. The total number of high-index facets increases significantly with the decreasing pore size. As shown in Fig. S5† the corresponding linear density of high-index facets increases from 0.67 nm^{-1}, 0.81 nm^{-1} to 1.04 nm^{-1} with pore size decreasing from 2 μm, 1.5 μm to 1 μm, respectively. The enhanced activity for MOR on Au micromeshes with smaller pore sizes can be attributed to preferential adsorption of OH_{ad}^-, and Au–$OH_{ads}^{(1-\lambda)-}$ on higher fractions of high-index facets.[6] The linear density of steps on Am-1 is ~1.04 nm^{-1}, which is much higher than 0.59 nm^{-1} on the best reported nanoporous Au,[8] and such a high density of steps is critical to the high performance of our Au meshes.

As we have introduced, based on the "d-band centre theory", tensile strain on Au can enhance the surface adsorption and improve the electrocatalytic activity of Au.[8,11,39] In a reported TEM study on nanoporous Au, an out-of-plane tensile strain is observed by nanobeam electron diffraction (NBD).[8] The authors attributed the excellent MOR performance of their nanoporous Au to the tensile strain.[8] Here we also performed NBD on the edge and centre of our Au micromeshes and observed the out-of-plane tensile strain. As shown in Fig. 4d, the tensile strain on local surface planes is indicated by the elongated NBD spots perpendicular to their local surface planes. In contrast, the NBD pattern from the centre part of the micromeshes does not show streaked spots, which means that no tensile strain exists in the interior of Au micromeshes. This is reasonable, because the middle part of strips is often a neutral plane even if a structure is highly deformed.

The stability of our most active sample, Am-1, is shown in Fig. 3d, where 90% of the activity still retains after 500 cycles between 0.85 V to 1.6 V because of the retention of steps, kinks, twins, stacking faults, and dislocations in Au micromeshes (Fig. S6a and b†). The stability is much better than those of
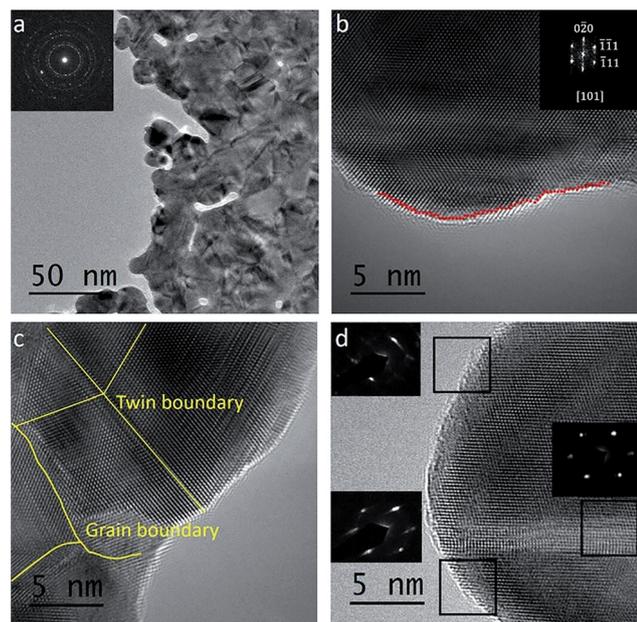

Fig. 4 Surface atomic structure of Au micromeshes sample. (a) Low magnification TEM image of Au micromeshes. The diffraction pattern (inset) shows that the Au micromeshes are polycrystalline. Typical Au micromeshes HRTEM image and FFT results (inset). (b) High-index planes appear on the surface area, and (c) grain boundary, twin boundary, stacking faults, steps and kinks are observed. (d) Nanobeam electron diffraction (NBD) patterns on two surfaces. Viewing along the [101] zone axis, the elongate spots are perpendicular to the local surface plan.

other reported nanostructured Au, such as nanoporous Au nanoparticles with 150 nm particle sizes, whose peak current density decreases to 64% after 480 cycles.[5] The number density of steps, kinks, twins, stacking faults, and dislocations in cycled Au micromeshes is reduced to 0.97 nm^{-1}, which is due to the increased radius of curvatures on the surface of Au micromeshes after cycling (Fig. S6c and d†).

Conclusions

In summary, we have developed a template method to fabricate large area 2D Au micromeshes. The Au micromeshes with pore diameters of 1 to 2 µm are studied. The MOR electrocatalytic activity, with a peak density of 0.264 mA cm^{-2} and an onset potential of 0.85 V, is among the best in Au electrocatalysts. Over 90% of the activity still retains after 500 cycles between 0.85 and 1.6 V. Under TEM, we characterized high density surface defects, such as steps, kinks, twins, stacking faults, and dislocations, and found that the on-edge high-index facets with low-coordination number located on the surface defects may be responsible for the high electrocatalytic performance. By quantifying the high density of steps and kinks on the exposed surfaces of Au micromeshes, the highest linear density of the steps and kinks is ~1.04 nm^{-1} in Au micromeshes with a pore size of 1 µm, which is significantly higher than that in nanoporous Au. The tensile strain caused by the edge effect applied on the out-most atomic layers could also enhance the absorbability of intermediates and the activity. Our method of fabricating micromesh structure offers a new way to design other 2D micromeshes polycrystalline metals for various electrode applications.

Acknowledgements

References

1 C.-J. Zhong and M. M. Maye, *Adv. Mater.*, 2001, **13**, 1507–1511.

2 L. D. Burke and P. F. Nugent, *Gold Bull.*, 1998, **31**, 39–50.

3 J. E. Bailie and G. J. Hutchings, *Chem. Commun.*, 1999, 2151–2152.

4 C. F. Guo, T. Sun, Q. Liu, Z. Suo and Z. Ren, *Nat. Commun.*, 2014, **5**, 3121.

5 S. Pedireddy, H. K. Lee, W. W. Tjiu, I. Y. Phang, H. R. Tan, S. Q. Chua, C. Troadec and X. Y. Ling, *Nat. Commun.*, 2014, **5**, 4947.

6 J. Zhang, P. Liu, H. Ma and Y. Ding, *J. Phys. Chem. C*, 2007, **111**, 10382–10388.

7 Y. Song, T. Miao, P. Zhang, C. Bi, H. Xia, D. Wang and X. Tao, *Nanoscale*, 2015, **7**, 8405–8415.

8 T. Fujita, P. Guan, K. McKenna, X. Lang, A. Hirata, L. Zhang, T. Tokunaga, S. Arai, Y. Yamamoto, N. Tanaka, Y. Ishikawa, N. Asao, Y. Yamamoto, J. Erlebacher and M. Chen, *Nat. Mater.*, 2012, **11**, 775–780.

9 Y. Ding and Z. Zhang, in *Springer Handbook of Nanomaterials*, ed. R. Vajtai, Springer, Verlag Berlin Heidelberg, 2013, vol. 1, pp. 779–818.

10 L. H. Qian and M. W. Chen, *Appl. Phys. Lett.*, 2007, **91**, 083105.

11 C. Bi, C. Feng, T. Miao, Y. Song, D. Wang and H. Xia, *Nanoscale*, 2015, **7**, 20105–20116.

12 W. Wang, J. Zhang, S. Yang, B. Ding and X. Song, *ChemSusChem*, 2013, **6**, 1945–1951.

13 Z. Quan, Y. Wang and J. Fang, *Acc. Chem. Res.*, 2013, **46**, 191–202.

14 J. Lai, W. Niu, R. Luque and G. Xu, *Nano Today*, 2015, **10**, 240–267.

15 F.-S. Ke, B. Solomon, Y. Ding, G.-L. Xu, S.-G. Sun, Z. L. Wang and X.-D. Zhou, *Nano Energy*, 2014, **7**, 179–188.

16 H. Xia, Y. Ran, H. Z. Li, X. Tao and D. Wang, *J. Mater. Chem. A*, 2013, **1**, 4678.

17 A. Wittstock, V. Zielasek, J. Biener, C. M. Friend and M. Baumer, *Science*, 2010, **327**, 319–322.

18 Y. Ding and M. Chen, *MRS Bull.*, 2009, **34**, 569–576.

19 A. Wittstock, J. Biener and M. Baumer, *Phys. Chem. Chem. Phys.*, 2010, **12**, 12919–12930.

20 Y. Wang, Z. Liu, Y. Huang, B. Han and G. Yang, *Langmuir*, 2006, **22**, 1928–1931.

21 C. F. Guo, Y. Lan, T. Sun and Z. Ren, *Nano Energy*, 2014, **8**, 110–117.

22 C. F. Guo, Y. Chen, L. Tang, F. Wang and Z. Ren, *Nano Lett.*, 2016, **16**, 594–600.

23 K. A. Friedrich, F. Henglein, U. Stimming and W. Unkauf, *Colloids Surf., A*, 1998, **134**, 193–206.

24 S. Xiao, F. Xiao, Y. Hu, S. Yuan, S. Wang, L. Qian and Y. Liu, *Sci. Rep.*, 2014, **4**, 4370.

25 K. A. Assiongbon and D. Roy, *Surf. Sci.*, 2005, **594**, 99–119.

26 S. Koçak, Z. Dursun and F. N. Ertaş, *Turk. J. Chem.*, 2011, **35**, 711–722.

27 C. Yu, F. Jia, Z. Ai and L. Zhang, *Chem. Mater.*, 2007, **19**, 6065–6067.

28 A. Nilsson, L. G. M. Pettersson, B. Hammer, T. Bligaard, C. H. Christensen and J. K. Nørskov, *Catal. Lett.*, 2005, **100**, 111–114.

29 N. Lopez, T. V. W. Janssens, B. S. Clausen, Y. Xu, M. Mavrikakis, T. Bligaard and J. K. Nørskov, *J. Catal.*, 2004, **223**, 232–235.

30 B. Hammer and J. K. Nørskov, *Surf. Sci.*, 1995, **343**, 211–220.

31 S. Schnur and A. Groß, *Phys. Rev. B: Condens. Matter Mater. Phys.*, 2010, **81**, 033402.

32 P. H. Citrin, G. K. Wertheim and Y. Baer, *Phys. Rev. B: Condens. Matter Mater. Phys.*, 1983, **27**, 3160.

33 C.-Y. Chiu, P.-J. Chung, K.-U. Lao, C.-W. Liao and M. H. Huang, *J. Phys. Chem. C*, 2012, **116**, 23757–23763.

34 C. Badan, M. T. M. Koper and L. B. F. Juurlink, *J. Phys. Chem. C*, 2015, **119**, 13551–13560.

35 Q. Zhang and H. Wang, *ACS Catal.*, 2014, **4**, 4027–4033.

36 J. Hernández, J. Solla-Gullón, E. Herrero, A. Aldaz and J. M. Feliu, *Electrochim. Acta*, 2006, **52**, 1662–1669.

37 J. A. Zimmerman, C. L. Kelchner, P. A. Klein, J. C. Hamilton and S. M. Foiles, *Phys. Rev. Lett.*, 2001, **87**, 165507.

38 Y. Lu, J.-p. Tu, C.-d. Gu, X.-h. Xia, X.-l. Wang and S. X. Mao, *J. Mater. Chem.*, 2011, **21**, 4843.

39 S. Xie, S. I. Choi, N. Lu, L. T. Roling, J. A. Herron, L. Zhang, J. Park, J. Wang, M. J. Kim, Z. Xie, M. Mavrikakis and Y. Xia, *Nano Lett.*, 2014, **14**, 3570–3576.